Enhanced Self-Healing in Dual Network Entangled Hydrogels by Macromolecular Architecture and Alignment of Surface Functionalized hBN Nanosheets

Chirag R. Ratwani,* Katarzyna Z. Donato, Sergey Grebenchuk, Alice Mija, Kostya S. Novoselov, and Amr M. Abdelkader*

Hydrogels have shown great promise as versatile biomaterials for various applications, ranging from tissue engineering to flexible electronics. Among their notable attributes, self-healing capabilities stand out as a significant advantage, facilitating autonomous repair of mechanical damage and restoration of structural integrity. In this work, a dual network macromolecular biphasic composite is designed using an anisotropic structure which facilitates unidirectional chain diffusion and imparts superior self-healing and mechanical properties. The resulting nanocomposite demonstrates significantly higher self-healing efficiency (92%) compared to traditional polyvinyl alcohol (PVA) hydrogels, while also improving the tensile strength and elastic modulus, which typically compete with each other in soft materials. This improvement is attributed to enhanced barrier properties within the matrix due to the alignment of surface-functionalized 2D hBN nanosheets along the biopolymer scaffold. The insights gained from this research can be leveraged to develop advanced self-healing materials by using 2D nanofillers as "safety barriers" to define the movement of polymeric chains.

1. Introduction

Hydrogels have emerged as versatile biomaterials with tremendous potential for various applications, including tissue engineering,[1] drug delivery,[2] lubrication,[3] and flexible electronics.[4] Among their remarkable features, self-healing is a significant advantage, as it allows for autonomous repair of mechanical damage and restoration of structural integrity.[5] In recent years, extensive research has been focused on developing self-healing hydrogels with enhanced efficiency and functionality.[6] Among all the known polymer matrices for self-healing hydrogels, poly(vinyl alcohol) (PVA) is the most explored polymer mainly due to its biocompatibility, high solubility in water, long-term stability, and ability to absorb large amounts of water.[7] PVA hydrogels are usually synthesized by physical crosslinking of PVA chains through multiple freeze-thaw cycles into a 3D interconnected polymeric network.[8]

However, pure PVA hydrogels' limited mechanical strength and healing properties impose limitations on their broader applications, especially in scenarios involving complex load-bearing requirements.[9] Moreover, the rise in local temperature due to

C. R. Ratwani, A. M. Abdelkader
Department of Design and Engineering
Faculty of Science & Technology
Bournemouth University
Poole, Dorset BH12 5BB, UK
E-mail: cratwani@bournemouth.ac.uk;
aabdelkader@bournemouth.ac.uk
K. Z. Donato
Centre for Advanced 2D Materials
National University of Singapore
Singapore 117546, Singapore

K. Z. Donato
Department of Inorganic Chemistry
Faculty of Science
Charles University
Hlavova 2030/8, Prague 128 00, Czech Republic
S. Grebenchuk
Department of Materials Science and Engineering
National University of Singapore
Singapore 117575, Singapore
S. Grebenchuk, K. S. Novoselov
Institute for Functional Intelligent Materials
National University of Singapore
Singapore 117575, Singapore
A. Mija, A. M. Abdelkader
Institut de Chimie de Nice
Université Côte d'Azur
UMR CNRS 7272
28 Av. Valrose, Nice 06108, France

**ADVANCED
SCIENCE NEWS**

www.advancedsciencenews.com

**ADVANCED
MATERIALS
INTERFACES**

www.advmatinterfaces.de

repetitive mechanical loading, caused by the inadequate heat transfer coefficient, especially in lubrication and biomedical applications, is one of the leading causes of failure in bare polymeric materials.[10,11] These temperature fluctuations can cause mechanical failure within the hydrogel and disrupt normal functioning. Many research works have tried to overcome these drawbacks by incorporating nanoparticles such as hydroxyapatite,[12] 1D carbon nanotubes,[13] 2D transition metal dichalcogenides like MoS$_2$,[14] and WS$_2$,[15] MXene,[16] hBN[17] and graphene[18] into the PVA matrix. The incorporation of 2D graphene oxide has been shown to improve the mechanical and self-healing properties to a large extent, mainly due to the oxygenated functionalities present on the surface. These functional groups play multiple roles. The first is to promote good adhesion between the graphene and PVA, allowing better load transfer on the matrix/filler interface.[19] The oxygenated groups also promote the homogeneous distribution of the graphene in the matrix and offer numerous hydrogen bonding sites that facilitate self-healing and reinforce the internal structure.
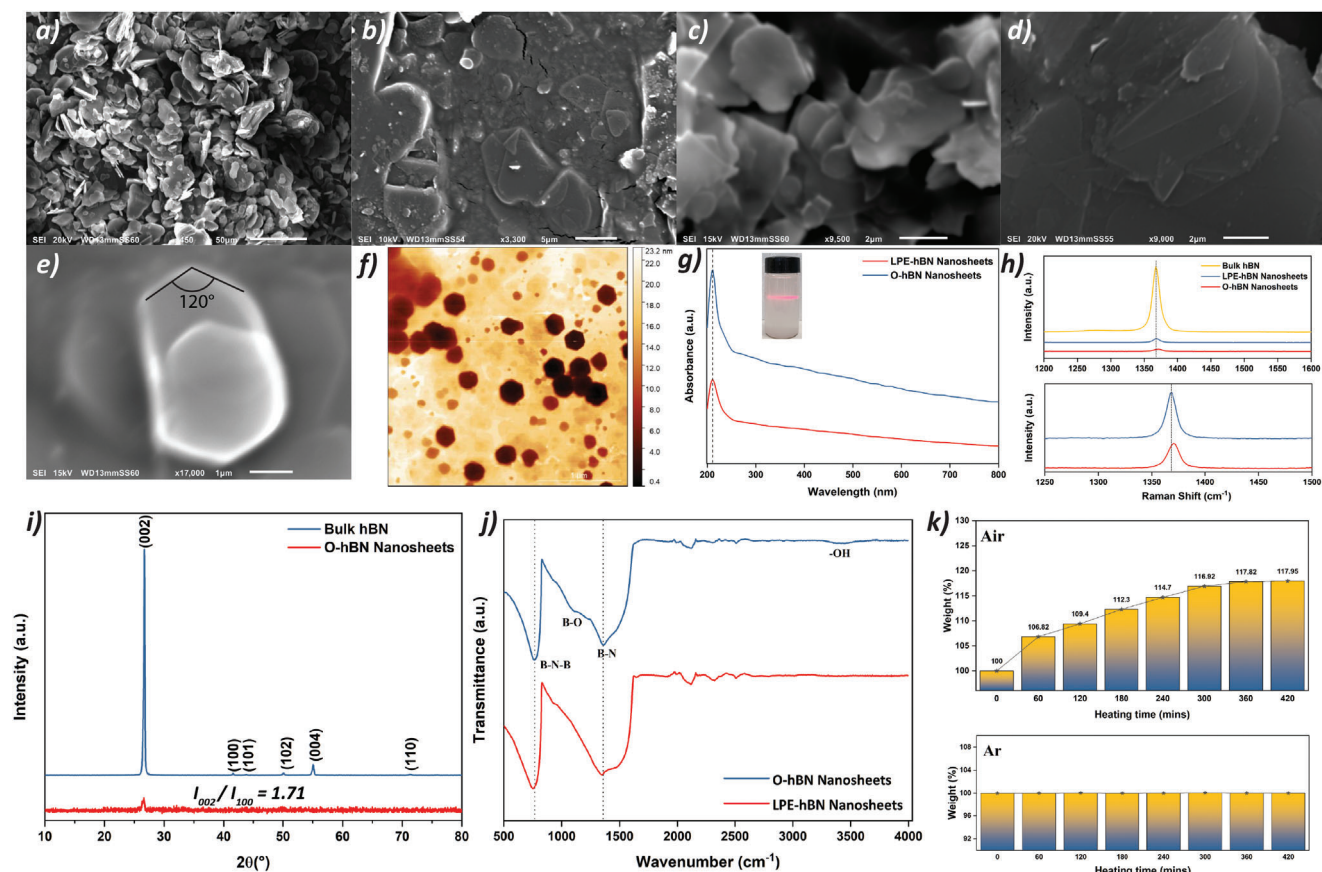
Regardless, graphene's dose-dependent cytotoxicity remains a significant concern, particularly in biomedical applications.[20,21] Interestingly, in vitro studies have indicated that oxidized graphene exhibits higher cytotoxicity than pristine graphene, making it even more difficult to incorporate into biocompatible composites.[22,23] Therefore, it is highly desirable to explore the development of alternative nanomaterials that can exhibit excellent bonding with the PVA matrix, similar to graphene oxide, while ensuring they are noncytotoxic in order to overcome the limitations associated with graphene-based materials in tissue engineering applications.[24]

2D hexagonal boron nitride (hBN), commonly referred to as white graphene, has gained significant recognition due to its remarkable electronic properties, exceptional chemical inertness, structural flexibility, thermal stability, high thermal conductivity, excellent electrical insulation, and outstanding biocompatibility.[25,26] Having mechanical and thermal properties comparable to graphene, hBN has demonstrated its ability to effectively enhance the mechanical and thermal characteristics of polymers. When hBN is incorporated into a polymer matrix, it can assist in healing for processes where heat is required to heal the material as hBN can provide additional thermal conductivity and assist in better dissipation.[27] However, when macromolecules have chains that are capable of undergoing segmental motion at room temperature, these nanosheets can hinder the chain mobility and retard the healing process.[28] This mandates the need for chemically bonding the hBN nanosheets to the host matrix where they can also participate in the healing chemistry. Previous studies have demonstrated that surface-functionalized hBN nanosheets can enhance the self-healing properties of composites by establishing reversible chemical bonds with the host matrix.[29,30] For instance, Cao et al. devised an epoxy coating based on the Diels-Alder mechanism, incorporating hBN nanosheets modified with maleimide groups.[31] These modified hBN nanosheets could form reversible cyclic adducts with the furan-based diene on the epoxy chains, resulting in a remarkable healing efficiency of 97.2% when subjected to heat-assisted healing. In another study, Jing et al. employed a two-step chemical oxidation process to synthesize hydroxylated hBN nanosheets with large lateral sizes.[32] These nanosheets were in-

tegrated into PVA hydrogel, leading to a significant enhancement in mechanical properties (43% increase) and thermal stability (45% increase) with a mere 0.12 wt.% nanosheet loading. The use of hBN nanosheets with functional groups that are compatible with the polymer matrix helps in better adhesion between the filler and the matrix, resulting in more efficient load transfer. Due to the inert nature of hBN, these functional groups also offer bonding sites for reconnection during the healing process, thereby ensuring that the filler participates in the healing chemistry rather than just being physically present in the host matrix.

One of the primary reasons for the preference of 2D materials, such as hBN, in composites is their exceptional in-plane properties. Luo et al. noted that aligning 2D materials within a hydrogel matrix through directional freezing can lead to further enhancements in mechanical properties.[33] This improvement is achieved through precise control of macromolecular architecture, resulting in anisotropic structures. Additionally, Qi et al. demonstrated that well-aligned hBN nanosheets serve as exponential layer-by-layer assemblies, effectively controlling diffusion in undesired directions by forming a "seal."[34] However, most of such studies lack in quantifying the key properties in different directions. The introduction of anisotropic structures can also facilitate the formation of channels to direct chain movement during the healing process. In self-healing hydrogels, healing typically requires the diffusion and reattachment of polymer chains across a damaged interface to restore mechanical integrity. In isotropic (randomly oriented) structures, this diffusion can be slow and inefficient due to the chaotic entanglement of chains, which creates resistance to movement. However, in anisotropic structures, the guided movement ensures that chains from opposing sides of the damage zone can diffuse more efficiently and reconnect.

This study uses three concurrent strategies to develop biphasic nanocomposites with anisotropic structures, showcasing enhanced mechanical strength and healing capabilities. First, hBN nanosheets were synthesized and functionalized through a scalable air oxidation process, followed by gentle liquid-phase exfoliation. This process facilitated the introduction of essential hydrogen-bonding sites onto bulk BN crystals while concurrently achieving the desired 2D morphology. Second, agar was utilized as a scaffold to orient the functionalized hBN nanosheets, thereby enhancing the mechanical properties and healing potential of the hydrogel. Agar, composed of agarose and agaropectin, offers structural versatility and exceptional biocompatibility, thereby improving mechanical stability when incorporated into another polymer matrix.[35,36] Additionally, the abundance of hydrogen-bond acceptor and donor sites along agar chains ensures multiple bonding sites for enhanced healing during the recovery process. Lastly, unidirectional freezing was employed to align the nanosheets within the gel phase, facilitating the formation of anisotropic structures to exploit the direction-dependent properties of 2D hBN. This synergistic approach yielded nanocomposite hydrogels with outstanding mechanical properties and remarkable healing efficiency of ≈92%, achieved with agar concentrations below 2 wt.% and O-hBN concentrations below 0.5 wt.%, without the need for additional crosslinking agents or compromising on elastic modulus. The observed enhancements in healing properties and water retention within the hydrogels can be attributed to the formation of horizontal barriers within the matrix, which effectively seal against water leakage and restrict the

**ADVANCED
SCIENCE NEWS**

www.advancedsciencenews.com

**ADVANCED
MATERIALS
INTERFACES**
Open Access

www.advmatinterfaces.de

Figure 1. SEM images of a) bulk hBN powder b) exfoliated O-hBN nanosheets c) O-hBN nanosheets cluster d) O-hBN nanosheets showing distinct layers e) single O-hBN nanosheets marked with vertex angle f) AFM topography image of O-hBN g) UV–vis spectra with dispersion showing Tyndall effect in inset h) comparative Raman spectra i) XRD diffractogram j) FT-IR spectra k) weight profile by thermogravimetric studies after heating at 1000 °C.

movement of polymeric chains in undesired directions during the healing process. Given that this process exclusively utilizes physical methods and incorporates biocompatible materials, the resulting hydrogels hold promise for safe utilization in biomedical applications and adaptable wearable technologies.

2. Results and Discussion

The first glimpse of the ability of the air oxidation process to exfoliate bulk hBN crystals, shown in **Figure 1a**, can be elucidated from the scanning electron microscopy (SEM) and transmission electron microscopy (TEM) analysis. In contrast to the initial hBN powder's sizable, thick crystals, the resultant materials exhibit a nanosheet structure with near transparency to the 10–20 kV electron beam, as depicted in Figure 1b. These nanosheets can be seen as aggregated, thin, and folded structures. The SEM images suggest successful exfoliation, revealing nanosheets with substantial lateral dimensions, ranging from 0.6 to 7 µm as per Figure 1c,d. Comparative assessment with prior research studies shows that the flake size obtained in this study is significantly higher. The edge of the nanosheets shows the typical hexagonal structure with a vertex angle of 120° (Figure 1e), suggesting no phase transformation occurs during the temperature treatment. The TEM image in Figure S1 (Supporting Information) shows

an aggregated but exfoliated cluster of nanosheets. The large lateral size and the low thickness of the nanosheets, as revealed by SEM and TEM images, favor their use in polymer composite applications. This quality imparts a positive influence on composite reinforcement and thermal transport properties. The lateral size is still much smaller than the precursor used as during the air oxidation process, oxygen atoms are introduced into the basal plane of the hBN crystals, forming B—O bonds. Upon immersion in hot water, these bonds undergo hydrolysis, leading to the exfoliation of bulk hBN into O-hBN nanosheets. The introduction of oxygen weakens the structural integrity of the basal plane, causing it to cleave into smaller sheets.

Atomic force microscopy (AFM) was performed for the nanosheets obtained after air oxidation, washing, and sonication to get more insight into the flakes' morphology. Figure S2a (Supporting Information) shows an optical image of O-hBN crystals highlighted on the substrate. The histogram in the inset shows the lateral size distribution collected for ≈140 flakes. It can be seen that the average lateral size for the nanosheets is ≈1 µm, with ≈2% being as big as 10 µm. The high magnification images in Figure S2b (Supporting Information) show translucent atomically thin layers. The topography images in Figure 1f show nanosheets with thickness in the range of 1–23 nm, with a large number of them on the lower side. Most of the flakes have a

2400691 (3 of 11)

clearly visible 120° vertex angle typical to the hexagonal crystals of hBN. High magnification AFM topography images in Figure S3 (Supporting Information) show the formation of well-exfoliated flakes, with Figure S3 (Supporting Information)(inset) showing the few-layer nature of the synthesized material. An AFM line scan on the magnified nanosheet in Figure S4a,b (Supporting Information) shows a height of under 10 nm at the thickest region, confirming the few-layer nature of the exfoliated nanosheets. A magnified topography image of isolated nanosheets (Figure S5a, Supporting Information) shows the flake edge, and when a phase image on the same was obtained (Figure S5b, Supporting Information), it shows a positive change in the phase shift at the edges. A positive shift may indicate increased stiffness within the lattice structure, possibly due to partial edge functionalization introduced during the air oxidation process.[37] This confirms that the oxidation primarily occurs from the lateral direction and hence higher number of H-bonding sites are present at the edges. This is in line with electron energy loss spectroscopy (EELS) results obtained by Jing et al., which show that edges in hBN are more susceptible to oxidation.[32]

The chemical changes on the surface of the O-hBN nanosheets were studied first. Figure 1g illustrates the UV–vis spectra of liquid-phase exfoliated hBN (LPE-hBN) nanosheets obtained through standard liquid exfoliation, as well as O-hBN produced after functionalizing hBN crystals in air. Both LPE-hBN and O-hBN exhibit an absorption peak at 210 cm. Still, the intensity of the former is significantly lower than the latter, indicating successful chemical modification of the nanosheets. Notably, even though the O-hBN has a very large lateral size, a very high concentration of nanosheets (0.74 mg mL^{-1}) can be obtained in the liquid. The cloudy dispersions of compound O-hBN exhibit a prominent Tyndall effect, as shown in Figure 1g inset, which is observed by the defocusing of the laser beam when observed under a low-powered red laser (650 nm).[38] The remarkable stability of the produced suspension in water for over three months suggests improved surface properties for increased dispersibility of O-hBN nanosheets in a hydrogen bond-rich environment as evidenced by Figure 1g inset. An extended time-dependent UV–vis spectroscopy study was conducted to analyze the stability of the dispersions over 24 h. The spectra shown in Figure S6 (Supporting Information) indicate that the dispersions remained stable throughout this period.

Following the thermal treatment process, agitating the substance in deionized water for several minutes induces a notable visual increase in viscosity, possibly due to the thermal decomposition and dissolution of boric acid formed during the heating process and subsequent hydrolysis of the treated hBN, leading to the formation of O-hBN.[39] These hydroxylated boron nitride sheets disperse within the aqueous solution without necessitating sonication; nevertheless, mild bath sonication is applied to expedite the suspension formation kinetics.

Raman spectroscopy of bulk hBN crystals in Figure 1h exhibits a distinct E_{2g} phonon mode vibration characterized by a sharp peak at 1367 cm^{-1}.[40] In comparison, a control sample of LPE-hBN nanosheets obtained through liquid phase exfoliation of bulk crystals was subjected to Raman analysis, revealing a significantly lower intensity (14 times less) of the E_{2g} phonon mode vibration. This lower intensity indicates the exfoliation of the crystals into few-layer nanosheets.[26] This exfoliation process

reduces the mass density of the LPE-hBN nanosheets by creating additional spaces between the layers, unlike the more densely packed unexfoliated h-BN bulk materials resulting in weaker E_{2g} vibrations. This is used as a control sample, and it facilitates the comparison of Raman spectra obtained from few-layer O-hBN nanosheets produced through high-temperature air functionalization and to confirm if Raman changes are brought in by exfoliation or by functionalization. Upon functionalization of BN nanosheets through the high-temperature air process, a similar low intensity of the E_{2g} phonon mode vibration is observed. However, when compared to LPE-hBN there is a notable blue peak shift of ≈2 cm^{-1}, confirming functionalization occurred on the crystal plane of the nanosheets.

To investigate the effect of the exfoliation process on the crystalline structure of hBN samples, X-ray diffraction (XRD) measurements were conducted on powdered specimens of both bulk hBN and O-hBN, as shown in Figure 1i. The obtained diffraction pattern reveals characteristic peaks corresponding to hBN crystals along three lattice directions: (002) and (004) in the *c*-axis direction, (101) and (102) in the diagonal direction, and (100) in the *a*-axis direction.[36] Typical to layered bulk materials, a higher intensity of the (002) peak is seen in all the samples, which indicates the powder's inclination to align its basal plane parallel to the sample's free surface. Hence, the ratio of (002) peak intensity to the intensity of peaks in other directions, like (100), can be a good measurement to give an idea about the orientation of hBN planes. As anticipated for 2D materials derived from exfoliation, a discernible yet weak diffraction pattern featuring characteristic peaks is evident. Notably, there is an observable broadening of the (002) peak in the diffractogram, while the peak position remains unchanged. Typically, functionalization causes a peak shift to lower 2θ values in XRD, indicating increased interlayer spacing due to attached functional groups. However, in the air oxidation of hBN, oxygen replaces nitrogen within the basal plane rather than attaching as dangling groups, which does not affect the interlayer spacing. This has been shown by in situ air oxidation studies using synchrotron radiation, where no peak shift occurs.[41] This observation implies that the insertion of O atoms occurs within the basal plane of the nanosheets, as opposed to acting as dangling functional groups extending from the plane. The latter case would typically increase the d-spacing, a phenomenon commonly associated with the functionalization of 2D materials.

Fourier transform infrared (FT-IR) spectroscopy was utilized to investigate the chemical changes occurring in BN after functionalization, and the recorded spectra are shown in Figure 1j. Before functionalization, the BN spectra exhibited distinct features, such as a characteristic B-N stretching signal at 1361 cm^{-1}, resulting from in-plane vibrations, as well as an out-of-plane bending signal at 772 cm^{-1} arising from B—N—B bonds. Upon heating, oxygen from the surrounding air led to the formation of B—O bonds.[42] This was evident from the appearance of a peak at 3200 cm^{-1} corresponding to B—O—H and a weak, broad shoulder ≈1150 cm^{-1} indicative of B—O bonds. Notably, loss of the B—O peak is not observed even after repeated washing with water, which is quite in contrast with previously reported works, thereby indicating its resistance to complete removal.[35] Additionally, FT-IR spectroscopy indicates the absence of remaining boron oxide or boric acid on the nanosheets after the functionalization process. These results support the previous hypothesis that

ADVANCED
SCIENCE NEWS

www.advancedsciencenews.com

ADVANCED
MATERIALS
INTERFACES

www.advmatinterfaces.de

during the high-temperature treatment of hBN nanosheets, the N atoms from the hBN lattice are substituted by O atoms. Subsequently, these O atoms undergo hydrolysis when the nanosheets are quenched in boiling water.

Advanced surface characterization by using X-ray photoelectron spectroscopy (XPS) has also been performed as shown by survey scan in Figure S7a (Supporting Information) and high-resolution spectra in Figure S7b,c (Supporting Information) for B1s and N1s. The deconvolution of B1s spectra shows the presence of a B—N peak at 191.1 eV and a B—O peak at 191.8 eV, while the N1s spectra show nitrogen is only bound to boron and no N-O or other nitrogen bonds are present.[43] The ratio of the peak area for B—O and B—N peaks is almost 1:5, significantly higher than previously reported results in the literature.[36] These results add more evidence to support that O has replaced N in the in-plane structures of hBN. Otherwise, peaks of B—O—N or O—N should be detected since the off-plane oxygen groups are likely to link with N.

hBN exhibits remarkable thermal stability, exhibiting negligible oxidation effects when exposed to temperatures up to 800 °C. However, as the temperature escalates, hBN undergoes a weight increase due to incorporating O atoms into its structural framework. The oxidation kinetics demonstrate a direct correlation with temperature, escalating correspondingly with this thermal parameter. Furthermore, the oxidation rate is also linearly proportional to the duration of heating. Through thermogravimetric investigations shown in Figure 1k, it was ascertained that prolonged heating under ambient conditions yields a progressive weight gain, which subsequently levels off following ≈6 h of heating in air at 1000 °C. This stabilization in weight gain could be attributed to the exhaustion of available sites susceptible to oxidation, which agrees with previous in situ studies.[41] Notably, subjecting hBN to heating in an Ar environment precludes any discernible weight gain, owing to the absence of an oxygen-enriched medium.

Motivated by the successful exfoliation and functionalization, O-hBN nanosheets, characterized by a strong affinity for hydrogen bond-rich environments, were employed in the synthesis of nanocomposite hydrogels through a combination of solution blending and directional freezing followed by freeze-thaw cycling. This process facilitates the alignment of nanosheets and induces crystallization within the macromolecular structure. The morphology of the resulting nanocomposite hydrogels was investigated through SEM. An optical image of PAB-0.3 shown in Figure S8 (Supporting Information) also shows the unidirectional arrangement of fibers along the direction of freezing. It should be noted that the samples were dried by lyophilization before examination. **Figure 2a** presents a SEM image of a bare PVA hydrogel, revealing irregular aggregates of PVA on the surface attributed to partial crystallization induced during the freeze-thaw process. The structural analysis reveals a nearly nonporous configuration, primarily attributed to matrix shrinkage during freeze-drying. Integration of PVA with agar and O-hBN introduces agar as an embedded phase, serving as a scaffold for O-hBN attachment. During directional freezing, the O-hBN nanosheets align parallel to the direction of ice crystal growth within a vertical mold, resulting in a macrostructure with a high concentration of in-plane O-hBN nanosheets. In Figure 2b,c, the presence of 0.3 wt.% O-hBN highlights agar's role as a scaffold for aligning

O-hBN nanosheets, while PVA chains form hydrogen bonds with agar and O-hBN, contributing to the overall structural integrity. Although most hBN nanosheets are enveloped by the polymeric matrix, making them less conspicuous in SEM images, hexagonal nanosheets, and in-plane aligned 2D flakes are discernible in Figure 2d,e. The arrows in Figure 2e highlight the predominant alignment of nanosheets in the plane. Upon increasing the O-hBN loading to 1 wt.%, the nanosheets tend to agglomerate, reducing the elastic properties. Upon stretching the PAB-1 sample, observable cleavage occurs from the nanosheet cluster, as seen in Figure 2f, indicating that the failure mechanism in these heavily loaded composites is associated with plane slipping among the O-hBN layers and inadequate adhesion between the 2D nanosheet clusters and the polymers. It is noteworthy that the examination of fractured surfaces was challenging due to the rapid action of hydrogen bonding mechanisms in such composites. These mechanisms swiftly form bonds with the freshly exposed cleaved sites, rich in hydrogen bond donor and acceptor sites. The SEM images in Figure 2g,h capture the agglomeration-induced cluster of nanosheets resulting from the high loading, illustrating the observed phenomena.

FTIR analysis was employed to investigate the bonding and composition of pure PVA and dual crosslinked hydrogels. In Figure 2i, a prominent and wide absorption peak can be seen at 3300–3400 cm^{-1} region, corresponding to the —OH stretching in PVA, agar, and O-hBN. The —CH_2 vibration peak, originating from the PVA chain backbone, is discernible in 2900–2940 cm^{-1} region, accompanied by robust stretching vibration peaks for C—O bonds in the 1000–1100 cm^{-1} range from PVA and agar. Distinctive β-1,4 glycosidic bonds, commonly present in agar and other natural cellulosic materials, are observable in the PAB-0 and PAB-0.3 hydrogels.[44] Despite the low concentration of O-hBN in the composite, a faint B—N vibration is distinguishable ≈1350–1380 cm^{-1}. Notably, this peak has shifted to a lower wavenumber compared to the O-hBN powder spectra, indicating the formation of hydrogen bonds between O-hBN nanosheets and macromolecular components of the nanocomposite hydrogel.[28] This confirms the proposed chemical bonding between the fillers and the matrix. Another noteworthy observation is that the intensity of C—O—H at 1650–1700 cm^{-1} follows the order PAB-0.3 > PAB-0 > PA_0B-0, suggesting enhanced water retention capacity in the composites compared to pure hydrogels. XRD diffractogram of PAB-0.3 nanocomposite hydrogel is further used to confirm the alignment of the O-hBN nanosheets. For hBN, the intensity ratio of peaks corresponding to crystallographic planes (002) and (100) can be used to understand the degree of in-plane orientation. The peak ratio I_{002}/I_{100} for the nanocomposite as shown in Figure 2j is 4.96, much higher than randomly oriented hBN nanosheets with I_{002}/I_{100} of 1.71 as shown in Figure 1i indicating higher in-plane orientation of O-hBN in the PAB-0.3 nanocomposite.

Water retention capacity was further verified by a gravimetric method where PVA-Agar hydrogels with varying quantities of O-hBN nanosheets were left open in a laminar flow cabinet with gentle airflow. As can be seen in Figure 2k, the addition of nanosheets significantly improves the ability of the matrix to trap water compared to pure PVA. The improved water retention could also be attributed to the chemisorption of water on the surface of O-hBN brought in by surface functionalization.
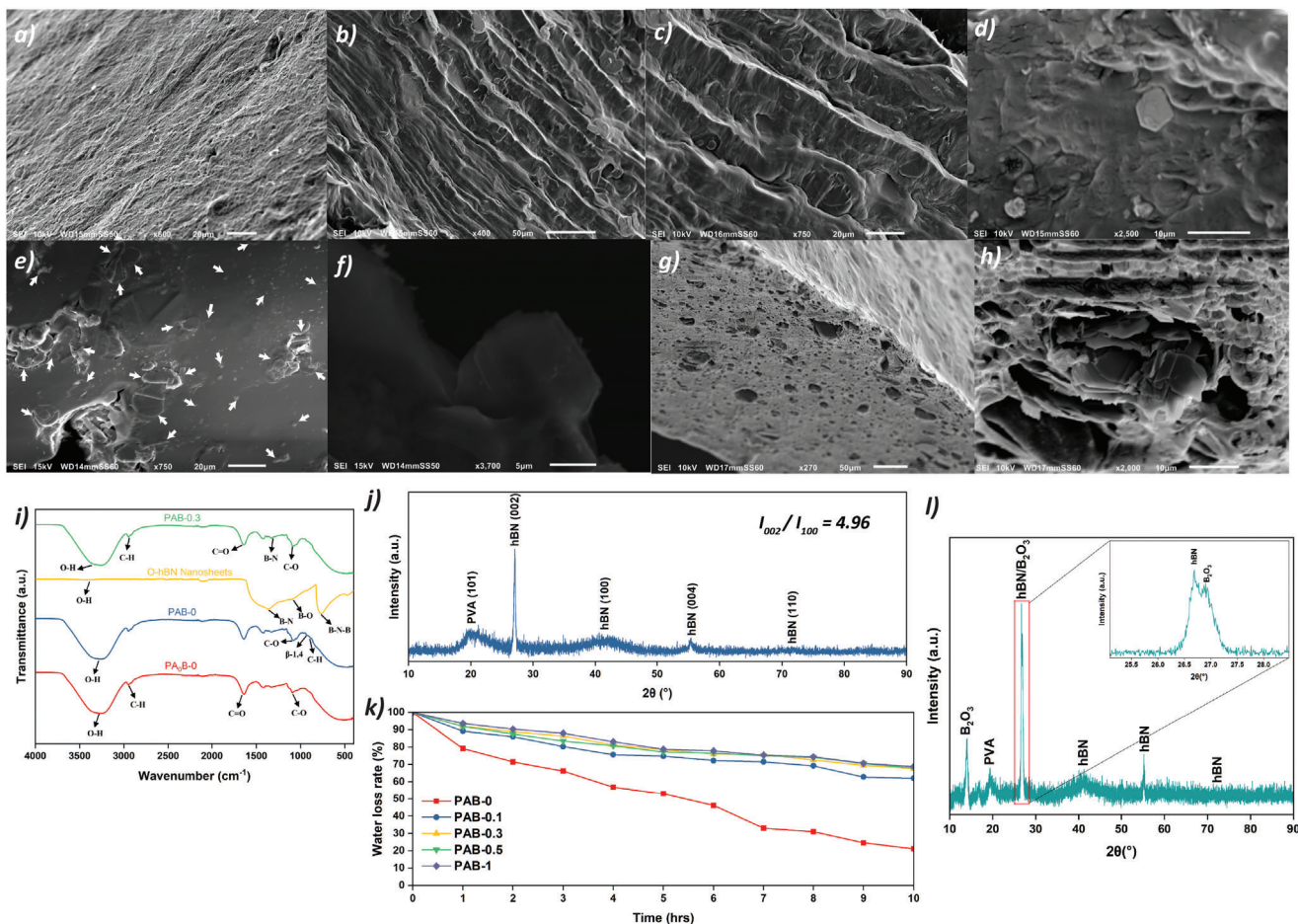
Figure 2. SEM imaging of a) pure PVA hydrogel b–d) PAB-0.3 hydrogel e) in-plane alignment of O-hBN nanosheets f) exposed O-hBN cluster at cleavage interface g,h) agglomeration of O-hBN nanosheets in PAB-1 i) FT-IR spectra of nanocomposite hydrogel j) XRD of PAB-0.3 k) Water retention capacity at different O-hBN concentrations l) XRD of nanocomposite hydrogel made with unwashed O-hBN.

Interestingly, due to the creation of a highly tortuous path along the z-axis (since the top face is predominantly responsible for drying) by the aligned nanosheets, higher loading of O-hBN nanosheets does not greatly influence the water retention.
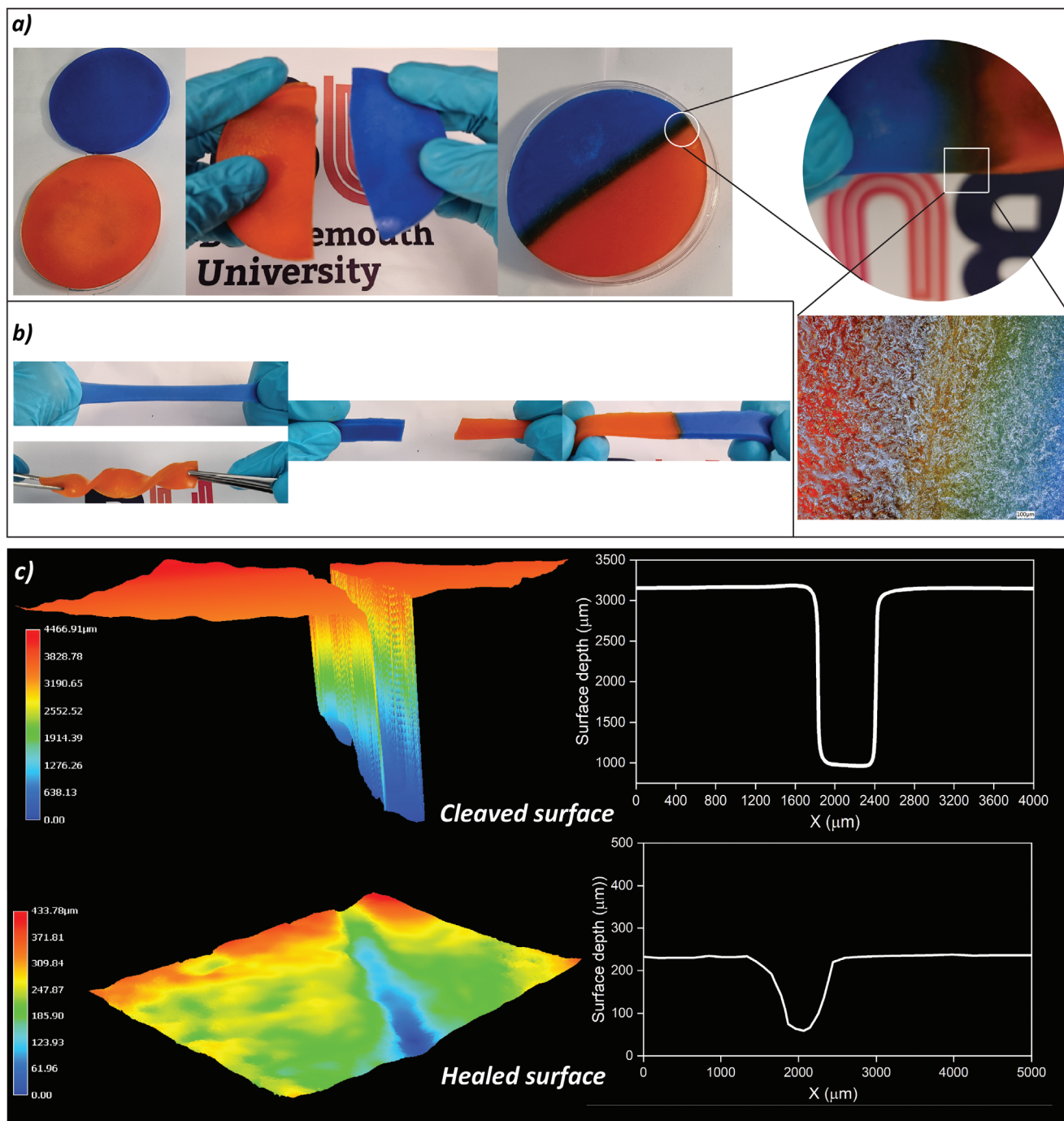
Further, to understand if the improved properties were brought in by the functionalization of hBN or by the presence of boron oxide, a control experiment without washing the nanosheets after air oxidation was conducted. The XRD analysis of this sample in Figure 2l shows the presence of B_2O_3 peaks, as expected. The composite samples made of the dry non-hydrated methods are very rigid as compared to samples with similar loadings of washed O-hBN, and it could barely hold their weight after healing; hence, it has not been considered for further analysis and highlights the importance of proper functionalization. Agar scaffold plays an important role in supporting O-hBN nanosheet alignment and improving the nanocomposite's mechanical properties.

A magnified SEM image of the Agar scaffold in the nanocomposite after drying the sample is shown in Figure S9 (Supporting Information). It can be observed that a large number of nanosheets, indicated by white arrows, are attached to the agar surface and are aligned in-plane along the lateral surface of Agar

without significant overlapping. Raman mapping was also attempted to determine the distribution of O-hBN in the composite based on the relative peak intensity. However, due to excessive fluorescence from Agar with a 532 nm laser, getting the sharp signals needed for accurate mapping was not feasible.

One of the key advantages achieved by using the directional freezing method was the improvement in self-healing properties. Nanocomposite samples along with artificial coloring were cast in disk-shaped molds and prepared by the method mentioned earlier into specimens as shown in **Figure 3a**. The hydrogels were cut into two pieces by using a sharp stainless-steel blade to cause the fracture and healing was initiated by keeping the broken pieces together under mild push. The healing process was allowed to occur for 24 h. without disturbing the pieces in the covered mold with restricted space. As can be seen in Figure 3b, after healing, the pieces are connected and can be stretched, twisted, or even subjected to tensile stress without breaking at the point of cleavage. Figure 3a also shows that the interface turns green (due to the mixing of orange and blue colorants) across the cut, suggesting the exchange of water and macromolecular components across the surface, suggesting macromolecular diffusion across the healing surface. The cleaved

ADVANCED
SCIENCE NEWS

www.advancedsciencenews.com

**ADVANCED
MATERIALS
INTERFACES**
Open Access

www.advmatinterfaces.de

Figure 3. a) Healing images of artificially dyed nanocomposite hydrogels and magnified image by optical microscope b) digital images showing processability and healing of hydrogel strips. c) Depth profiling of cleaved and healed surface.

surface was examined using an optical profilometer to investigate surface morphology and assess healing in recovered depth. Figure 3c presents heatmaps and depth profiles of the nanocomposite both before and after the healing process. Remarkably, the surface and bulk exhibit nearly complete recovery posthealing. Regions of the hydrogel surrounding the cut exhibit mild sagging, attributed to the reconnection of some hydrogen bonds on the same interface side. The gradual change of the colors of the

reconnection zone in the microscopic image also suggested diffusion of the materials across the healed cleavage. Depth profile analysis reveals a healing efficiency of 82.85%. However, it is essential to note that this method relies on visible light penetration for measurements, which may pose limitations. In reality, bulk healing may not have occurred, and the observed decrease in crack width could be a result of localized expansion or surface healing without full functional restoration. Hence, it is

2400691 (7 of 11)
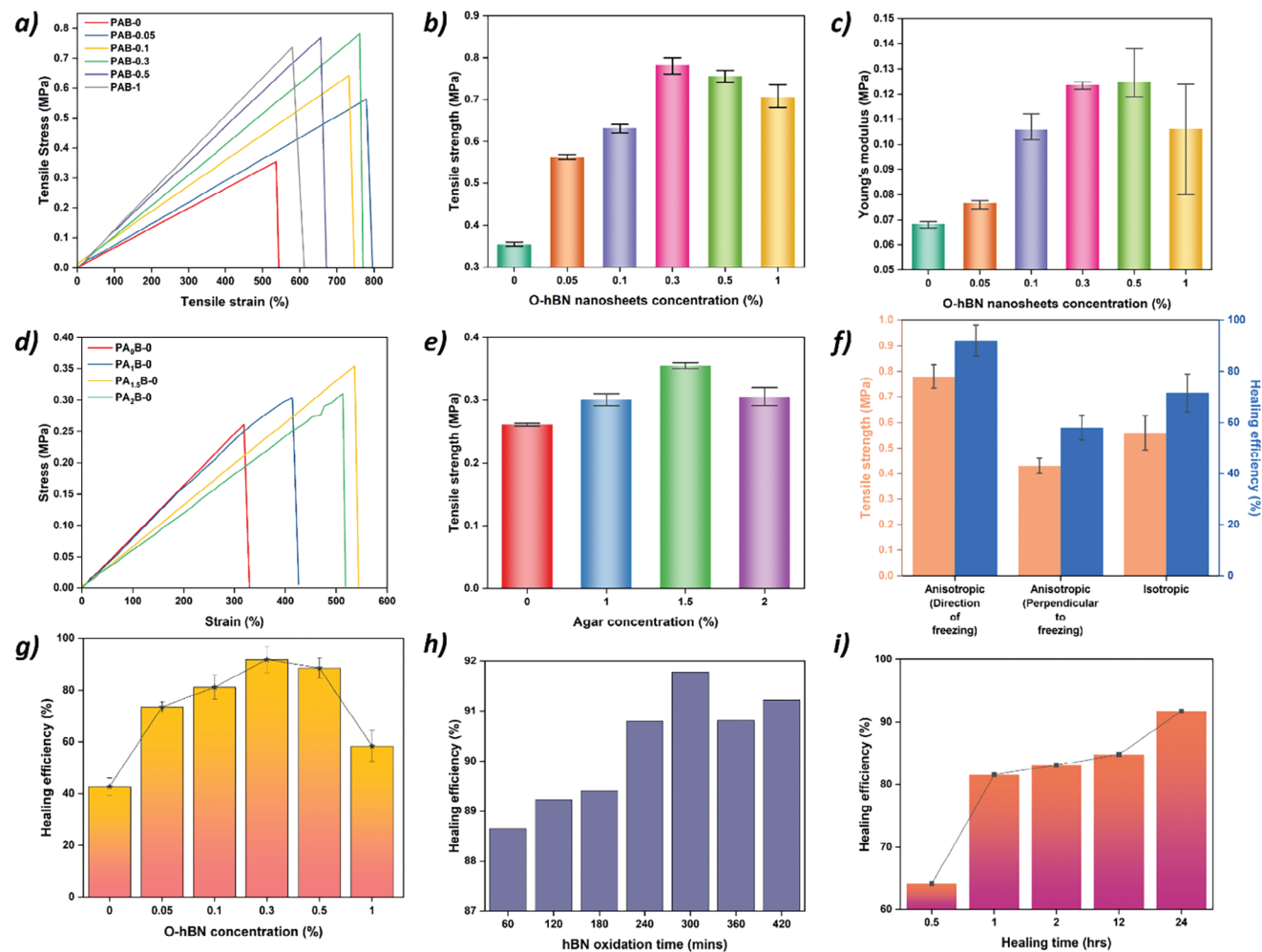
Figure 4. Mechanical and healing tests a) stress-strain curves at different O-hBN concentrations b,c) Tensile strength and Young's modulus comparison based on a). d) Stress-strain curves at different Agar loading. e) Tensile strength comparison on d). f) comparison of properties in different directions of anisotropic and isotropic hydrogels. g) effect of O-hBN concentration on healing efficiency h) effect of hBN oxidation time on healing efficiency i) effect of healing time on healing efficiency.

essential to signify the healing process by performing mechanical tests.

Then the mechanical properties of the composites using dog-bone-shaped specimens were measured as per the ASTM D412 standards. The obtained tensile test results, illustrated in **Figure** 4a, reveal that the tensile strength of the pristine PAB-0 hydrogel is ≈0.35 MPa. Notably, this tensile strength experiences a substantial increase to 0.78 MPa with the incorporation of 0.3 wt.% O-hBN nanosheets. However, an incremental rise in nanosheet concentration to 1 wt.% leads to structural brittleness, resulting in rupture at a comparatively lower loading. Optimal tensile strength is observed at a 0.3% loading of O-hBN, while the highest Young's modulus is attained at a 0.5% loading, as depicted in Figure 4b,c. To comprehend the contribution of the Agar component in the matrix, investigations were conducted by varying its quantity. Pure agar hydrogels proved fragile and could not undergo tensile tests independently, necessitating the inclusion of PVA to furnish a structural backbone. Notably, as seen in Figure 4d, adding merely

1.5% Agar by weight enhances the tensile strength of the hydrogel by ≈40%. Subsequent increments in Agar concentration resulted in diminished mechanical properties, likely due to insufficient PVA chains per unit volume to sustain the hydrogel under stretched conditions. As demonstrated in Figure 4e and Figure S10 (Supporting Information), the highest tensile strength and Young's modulus were observed at a 1.5% Agar concentration. Tensile strength and self-healing efficiency have been tested in both the parallel and perpendicular directions to the freezing axis along with an isotropic control sample. As shown in Figure 4f, the strength and healing efficiency in the freezing direction are significantly higher than in the perpendicular direction, due to the alignment of the nanosheets.

The investigation into self-healing properties involved cutting pieces of PAB-x hydrogels and subsequently joining them under gentle pressure for 24 h. It was observed that the sample featuring the optimum O-hBN concentration for mechanical strength also exhibited superior healing capabilities (as shown

**ADVANCED
SCIENCE NEWS**

www.advancedsciencenews.com

**ADVANCED
MATERIALS
INTERFACES**

www.advmatinterfaces.de

in Figure 4g), achieving an efficiency of 92%. Conversely, higher concentrations of O-hBN hindered healing, possibly due to impediments in chain movement arising from the nanosheet concentration beyond the scaffold. Further, it was also found that the healing efficiency of the composite is improved when it is reinforced with nanosheets with higher degree of functionalization (obtained by increasing the duration of air oxidation process), as evident by Figure 4h. The healing mechanism, predominantly governed by hydrogen bonding, displayed rapid kinetics, with ≈83% of healing occurring within the initial hour, as clear from Figure 4i. This observation underscores the nanocomposite's inherent ability to expedite healing processes without necessitating external stimuli aside from a gentle application of pressure. The properties of the synthesized nanocomposite are compared with results from the literature, as shown in Table S1 (Supporting Information), confirming a unique combination of high strength with high healing efficiency, unseen in previous similar works.

As shown in this work improvement in the self-healing ability and mechanical properties of the dual-network entangled hydrogels can be achieved by using surface functionalization to improve hydrogen bonding with hBN and using directional freezing to align the hBN nanosheets to improve the intrinsic healing properties of the hydrogel network. The improvements due to the improved interface and effective load transfer are revealed by mechanical and healing tests. Future work could explore fiber fillers with high aspect ratios such as cellulose nanofibrils to help align the 2D materials within the matrix, possibly giving further performance improvement.

3. Conclusion

This study demonstrates advancements in the self-healing capacity and mechanical characteristics of dual-network entangled hydrogels. These improvements are achieved through surface functionalization to enhance hydrogen bonding with hBN, the incorporation of an Agar scaffold to facilitate nanosheet alignment, and the application of directional freezing to effectively "seal" the hydrogel network. Notably, these enhancements hold promise for significant strides in the development of self-healing nanocomposites. Conventional reports in this domain predominantly feature healable networks with randomly dispersed 2D materials, limiting the exploitation of the exceptional properties of such materials in the X-Y plane. In contrast, our approach strategically leverages surface functionalization techniques to augment hydrogen bonding interactions with hBN, thereby optimizing the utilization of its unique properties within the X-Y plane. Moreover, the introduction of an Agar scaffold serves a pivotal role in aligning nanosheets directionally, imparting a degree of order to the hydrogel matrix while also reinforcing the macromolecular backbone of the composite. Furthermore, the application of directional freezing techniques serves as a transformative method to "seal" the hydrogel network. This process aids in the creation of a well-organized and robust structure, thereby fortifying the mechanical properties of the hydrogel. The directional freezing not only contributes to the enhanced mechanical strength but also promotes the creation of an organized network that facilitates efficient self-healing processes.
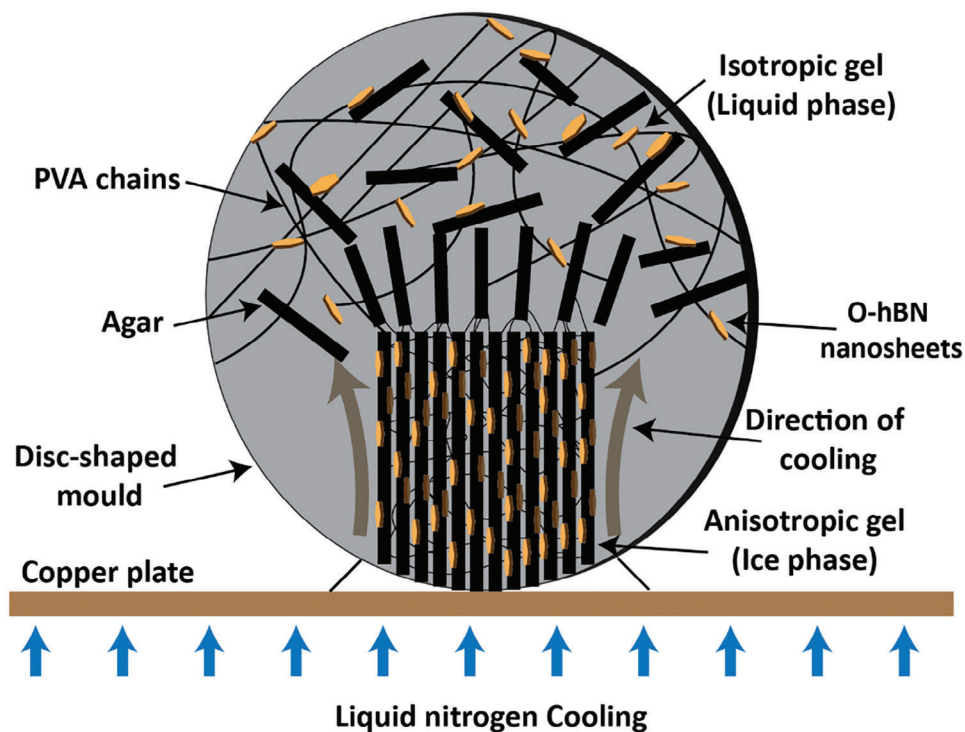
4. Experimental Section

Materials: hBN (powder, 15 μm) was used without further preparation. Agar (powder, microbiology grade) was purchased from Sigma-Aldrich, UK. Polyvinyl Alcohol (PVA, 98–99% hydrolyzed, Avg. MW: 57 000–66 000) and artificial coloring additives were purchased from Alfa Aesar. Double distilled water was used for all experiments. All reagents were used as sourced without further purification.

hBN functionalization by Air Oxidation: hBN functionalization was achieved through air oxidation at high temperatures.[39] In the process, 5 g of as received hBN powder (99.9% purity) was utilized and loaded into an alumina crucible, which was then placed in a tube furnace. The temperature gradually ramped up to 8 °C until it reached 1000 °C. Upon reaching the peak temperature, the sample was held for various durations to produce samples with different functional group loadings. The material was extracted at ≈200 °C during the cooling phase and rapidly quenched in hot water. Subsequently, it was continuously stirred in hot water for 1 h, followed by washing and centrifugation procedures repeated at least three times. The washed samples were then subjected to sonication in distilled water for a minimum of 30 min to form a milky white stable suspension of surface-functionalized hBN nanosheets. Sonication was performed using a bath sonicator, Fisherbrand, Elmasonic S30(H) 280W. The obtained nanosheet powder after drying this suspension is denoted as O-hBN. Depending on the duration of exposure of hBN powder at the peak temperature in the furnace, the yield of O-hBN nanosheets ranged from 0.62 to 0.74 g for every 1 g of bulk hBN crystals. A control sample of hBN nanosheets was prepared by liquid phase exfoliation (LPE) of bulk hBN crystals in low-boiling solvents using the method described in the literature.[45]

Synthesis of Dual Cross-Linked Nanocomposite Hydrogels: To synthesize nanocomposite hydrogels, a measured quantity of agar powder and O-hBN nanosheets were stirred in water for 12 h to allow the agar particles to swell and initiate hydrogen bonding between O-hBN and agar. Subsequently, PVA was added to the mixture, and water was supplemented to achieve the desired concentration. The beaker containing this mixture was covered and placed in an oil bath, where it was heated for 2 h at 95 °C to obtain a homogeneous solution. Afterward, the mixture was removed from the oil bath and sonicated for 20 min at an elevated temperature to remove any trapped air bubbles. It was carefully poured into leak-proof, disc-shaped PTFE molds and sealed after sonication. The molds were then positioned vertically on a copper surface and cooled using liquid nitrogen. Uni-directional cooling induced the crystallization of water molecules, with the crystals forming in an aligned manner following the direction of cooling. **Figure 5** illustrates the process of O-hBN nanosheets aligning along the agar macromolecular structure. The nanocomposites were subjected to two freeze-thawing cycles, freezing at −20 °C for 2 h and thawing at room temperature for 6 h, following the freezing process. All the nanocomposites are denoted by PAB-x, where the hydrogel is synthesized by 20 wt.% PVA, 1.5 wt.% Agar, and x shows the concentration of O-hBN unless stated otherwise.

Material Characterization: X-ray photoelectron spectroscopy (XPS) was performed using Kratos AXIS Supra+ with a step-size of 1 eV for the survey spectrum and 0.05 eV for high-resolution spectra, respectively. An ion gun was used to neutralize the charging phenomena. Data analysis and fitting were performed with ESCApe software after Shirley's background subtraction. Raman spectroscopy was conducted using a fully confocal Horiba XploRA spectrometer equipped with a green laser ($\lambda = 532$ nm) and a 50× objective lens. Testing parameters were adjusted to obtain the maximum signal-to-noise ratio. UV–vis spectra were acquired utilizing an Agilent Cary 60 UV–vis Spectrophotometer using Quartz cuvettes with a path length of 10 mm. Tecnai F20 TEM was used for the imaging of nanosheets. Powdered X-ray diffraction (XRD) analysis utilized Cu Kα radiation and was conducted with a Siemens D5000 diffractometer (Siemens, Germany). Atomic force microscopy (AFM) images of the sample topography were acquired using a Bruker Dimension Icon AFM operating in a tapping mode, employing Bruker RTESPA-150 cantilevers with a spring constant k of 5 N m^{-1}. Before the measurements, samples were mechanically exfoliated onto a SiO$_2$/Si substrate. Fourier transform infrared (FT-IR)

ADVANCED
SCIENCE NEWS

www.advancedsciencenews.com

ADVANCED
MATERIALS
INTERFACES
Open Access

www.advmatinterfaces.de

Figure 5. Schematic representation of directional freezing with alignment of hBN and macromolecular structure (not to scale). Black flakes represent Agarose structures and golden flakes represent hBN nanosheets.

spectra were obtained using a Platinum ATR—Alpha II FTIR spectrophotometer (Bruker, USA). Thermogravimetric analysis (TGA) was conducted using NETZSCH STA 409 PC/PG at a rate of 5 K min^{-1} in an Alumina crucible. Tensile testing was conducted on dog-bone-shaped hydrogel specimens prepared following ASTM D412 standards. It was carried out using a Universal testing machine Zwick/Roell Z030 equipped with an Xforce K$^+$ 10 kN load cell, maintaining a constant crosshead speed of 5 mm min^{-1}. Each sample was replicated five times, and the average result was considered the tensile strength for healing efficiency calculations. The dog-bone-shaped specimens were halved, and the two pieces were brought into contact to initiate hydrogen bond formation, remaining together for 2 h in ambient conditions. The healing efficiency was determined by calculating the ratio between the tensile strength of the healed sample and that of the pristine sample. High-resolution optical imaging and profilometric 3D images of samples were obtained using the Keyence VHX-5000 digital microscope (Keyence Corporation, Japan). JEOL JSM-6010 tungsten cathode scanning electron microscope was used to carry out scanning electron microscopy (SEM) image analysis of nanomaterials and composites.

Supporting Information

Supporting Information is available from the Wiley Online Library or from the author.

Conflict of Interest

The authors declare no conflict of interest.

Data Availability Statement

The data that support the findings of this study are available from the corresponding author upon reasonable request.

[1] S. Correa, A. K. Grosskopf, H. L. Hernandez, D. Chan, A. C. Yu, L. M. Stapleton, E. A. Appel, *Chemical Reviews* **2021**, *121*, 11385.

[2] P. Kesharwani, A. Bisht, A. Alexander, V. Dave, S. Sharma, *J. Drug Deliv. Sci. Technol.* **2021**, *66*, 102914.

[3] T. Shoaib, R. M. Espinosa-Marzal, *Coll. Interfaces* **2020**, *4*, 54.

[4] Y. Zhang, Y. Tan, J. Lao, H. Gao, J. Yu, *ACS Nano* **2023**, *17*, 9681.

[5] A. Devi V K, R. Shyam, A. Palaniappan, A. K Jaiswal, T.-H. Oh, A. J Nathanael, *Polymers* **2021**, *13*, 3782.

[6] C. R. Ratwani, A. R. Kamali, A. M. Abdelkader, *Prog. Mater. Sci.* **2023**, *131*, 101001.

[7] H. Adelnia, R. Ensandoost, S. Shebbrin Moonshi, J. N. Gavgani, E. I. Vasafi, H. T. Ta, *Eur. Polym. J.* **2022**, *164*, 110974.

[8] H. Zhang, H. Xia, Y. Zhao, *ACS Macro Lett.* **2012**, *1*, 1233.

[9] W. Li, D. Wang, W. Yang, Y. Song, *RSC Adv.* **2016**, *6*, 20166.

[10] Q. Xiao, W. Han, R. Yang, Y. You, R. Wei, X. Liu, *Polym. Compos.* **2018**, *39*, E1598.

[11] M. C. Galetz, C. Goetz, P. Adam, U. Glatzel, *Adv. Eng. Mater.* **2007**, *9*, 1089.

[12] M. B. Jalageri, G. C. Mohan Kumar, *Gels* **2022**, *8*, 555.

[13] L. Zhao, J. Zhang, P. Cao, L. Kang, Q. Gong, J. Wang, Y. Zhang, Q. Li, *Composites, Part B* **2021**, *211*, 108661.

[14] H. T. Zheng, Y. C. Zhang, X. He, H. H. Liu, A. Y. Chen, X. F. Xie, *J. Alloys Compd.* **2022**, *918*, 165801.

[15] C. R. Ratwani, S. Zhao, Y. Huang, M. Hadfield, A. R. Kamali, A. M. Abdelkader, *Small* **2023**, *19*, 2207081.

[16] C. R. Ratwani, D. Demko, B. Bakhit, A. R. Kamali, A. M. Abdelkader, *ACS Appl. Nano Mater.* **2024**, *7*, 20196.

[17] D. Aki, S. Ulag, S. Unal, M. Sengor, N. Ekren, C.-C. Lin, H. Yılmazer, C. B. Ustundag, D. M. Kalaskar, O. Gunduz, *Mater. Des.* **2020**, *196*, 109094.

[18] J. Ma, W. Du, Z. Chen, W. Wang, L. Zhang, *Macromol. Mater. Eng.* **2023**, *308*, 2200332.

[19] Y. Huang, M. Zhang, W. Ruan, *J. Mater. Chem. A* **2014**, *2*, 10508.

[20] N. Nasirzadeh, M. R. Azari, Y. Rasoulzadeh, Y. Mohammadian, *Toxicol. Industr. Health* **2019**, *35*, 79.

[21] C. R. Ratwani, T. Barkan, *Graph. 2D Mater.* **2024**, *9*, 3.

[22] X. Zhang, C. Wei, Y. Li, Y. Li, G. Chen, Y. He, C. Yi, C. Wang, D. Yu, *J. Biomed. Mater. Res., Part A* **2020**, *108*, 614.

[23] T. Barkan, C. R. Ratwani, D. Johnson, K. Thodkar, C. Hill, *Nat. Rev. Phys.* **2024**, https://www.nature.com/articles/s42254-024-00754-9.

[24] Q. Weng, B. Wang, X. Wang, N. Hanagata, X. Li, D. Liu, X. Wang, X. Jiang, Y. Bando, D. Golberg, *ACS Nano* **2014**, *8*, 6123.

[25] K. Zhang, Y. Feng, F. Wang, Z. Yang, J. Wang, *J. Mater. Chem. C* **2017**, *5*, 11992.

[26] M. J. G. Guimarey, C. R. Ratwani, K. Xie, M. Koohgilani, M. Hadfield, A. R. Kamali, A. M. Abdelkader, *Tribol. Int.* **2023**, *180*, 108264.

[27] M. G. Rasul, A. Kiziltas, B. Arfaei, R. Shahbazian-Yassar, *npj 2D Mater. Appl.* **2021**, *5*, 56.

[28] X. Gao, T. Deng, X. Huang, M. Yu, D. Li, J. Lin, C. Yu, C. Tang, Y. Huang, *Soft Matter* **2022**, *18*, 859.

[29] Y. Cao, J. Zhang, D. Zhang, Y. Lv, J. Li, Y. Xu, K. He, G. Chen, C. Yuan, B. Zeng, L. Dai, *J. Mater. Sci.* **2020**, *55*, 11325.

[30] Z. Shang, D. Ding, X. Wang, B. Liu, Y. Chen, L. Gong, Z. Liu, Q. Zhang, *Polym. Adv. Technol.* **2021**, *32*, 4745.

[31] Y. Cao, X. Wang, J. Wu, Y. Xu, J. F. Gerard, L. Jiang, B. Zeng, L. Dai, *Prog. Org. Coat.* **2022**, *173*, 107209.

[32] L. Jing, H. Li, R. Y. Tay, B. Sun, S. H. Tsang, O. Cometto, J. Lin, E. H. T. Teo, A. I. Y. Tok, *ACS Nano* **2017**, *11*, 3742.

[33] Q. Luo, Y. Shan, X. Zuo, J. Liu, *RSC Adv.* **2018**, *8*, 13284.

[34] X. Qi, X. Yang, J. Zhu, Y. Hou, M. Yang, *ACS Nano* **2016**, *10*, 9434.

[35] X. Sun, C. Luo, F. Luo, *Eur. Polym. J.* **2020**, *124*, 109465.

[36] K. Basumatary, P. Daimary, S. K. Das, M. Thapa, M. Singh, A. Mukherjee, S. Kumar, *Food Packag. Shelf Life* **2018**, *17*, 99.

[37] S. N. Magonov, V. Elings, M. H. Whangbo, *Surf. Sci.* **1997**, *375*, L385.

[38] A. M. Abdelkader, I. A. Kinloch, R. A. W. Dryfe, *ACS Appl. Mater. Interfaces* **2014**, *6*, 1632.

[39] Z. Cui, A. J. Oyer, A. J. Glover, H. C. Schniepp, D. H. Adamson, *Small* **2014**, *10*, 2352.

[40] R. V. Gorbachev, I. Riaz, R. R. Nair, R. Jalil, L. Britnell, B. D. Belle, E. W. Hill, K. S. Novoselov, K. Watanabe, T. Taniguchi, A. K. Geim, P. Blake, *Small* **2011**, *7*, 465.

[41] Z. Yan, A. Abdelkader, S. Day, C. Tang, C. Casiraghi, W. Mirihanage, *Nanotechnology* **2021**, *32*, 105704.

[42] H. Mazhar, D. H. Adamson, M. A. Al-Harthi, *Mater. Chem. Phys.* **2023**, *308*, 128243.

[43] C. R. Ratwani, D. Demko, B. Bakhit, A. R. Kamali, A. M. Abdelkader, *ACS Appl. Mater. Interfaces* **2024**, *16*, 5847.

[44] D. Qiao, W. Tu, L. Zhong, Z. Wang, B. Zhang, F. Jiang, *Polymers* **2019**, *11*, 1952.

[45] J. Shen, Y. He, J. Wu, C. Gao, K. Keyshar, X. Zhang, Y. Yang, M. Ye, R. Vajtai, J. Lou, P. M. Ajayan, *Nano Lett.* **2015**, *15*, 5449.